High viscosity environments: an unexpected route to obtain true atomic resolution with atomic force microscopy

Stefan AL Weber[1,2], Jason I Kilpatrick[1], Timothy M Brosnan[1,3], Suzanne P Jarvis[1,3] and Brian J Rodriguez[1,3]

[1]Conway Institute of Biomolecular and Biomedical Research, University College Dublin, Belfield, Dublin 4, Ireland
[2]Max Planck Institute for Polymer Research, Ackermannweg 10, 55128 Mainz, Germany
[3]School of Physics, University College Dublin, Belfield, Dublin 4, Ireland

E-mail: Stefan.Weber@mpip-mainz.mpg.de and Brian.Rodriguez@ucd.ie

Abstract

Atomic force microscopy (AFM) is widely used in liquid environments, where true atomic resolution at the solid–liquid interface can now be routinely achieved. It is generally expected that AFM operation in more viscous environments results in an increased noise contribution from the thermal motion of the cantilever, thereby reducing the signal-to-noise ratio (SNR). Thus, viscous fluids such as ionic and organic liquids have been generally avoided for high-resolution AFM studies despite their relevance to, e.g. energy applications. Here, we investigate the thermal noise limitations of dynamic AFM operation in both low and high viscosity environments theoretically, deriving expressions for the amplitude, phase and frequency noise resulting from the thermal motion of the cantilever, thereby defining the performance limits of amplitude modulation (AM), phase modulation (PM) and frequency modulation (FM) AFM. We show that the assumption of a reduced SNR in viscous environments is not inherent to the technique and demonstrate that SNR values comparable to ultra-high vacuum systems can be obtained in high viscosity environments under certain conditions. Finally, we have obtained true atomic resolution images of highly ordered pyrolytic graphite and mica surfaces, thus revealing the potential of high-resolution imaging in high viscosity environments.

1. Introduction

Atomic force microscopy (AFM) continues to be an enabling technology for the investigation of material properties, surface topography and tip-sample interactions, often with true atomic resolution. The ubiquity of the technique allows for the study of interactions at various interfaces in a wide range of environments including ultra-high vacuum (UHV), air and liquids. Generally, AFM experiments in liquid are performed in aqueous solutions as they provide a physiologically relevant environment for many biomolecular systems or because of their ability to enable easy tuning of the nature and length-scale of the tip-sample interactions. Nevertheless, AFM studies in non-aqueous liquid environments are also of great interest as they enable *in situ* investigations of various processes including chemical reactions [1], lubrication [2] and molecular ordering [3-5]. In particular, devices based on ionic liquid electrolytes have been proposed as promising systems for energy applications [6], often in combination with graphene as the electrode material [7-10]. Despite the scientific need for investigations into the interfacial and transport properties of such systems with high spatial resolution, AFM in highly viscous liquids remains underutilized.

With the continued development of low-noise AFM instrumentation [11] the thermal noise contribution of the cantilever has become the dominant factor in determining the signal-to-noise ratio (SNR). A reduction in the quality factor (Q) of a cantilever in fluid is associated with a higher contribution of thermal noise resulting in a reduced SNR and is generally expected to impede high-resolution imaging [12-14]. Despite these limitations, high lateral resolution AFM investigations in aqueous environments have been the subject of extensive studies and are indispensable for gaining insight into interactions at the solid–liquid interface [15-21]. However, many fluids of interest can have viscosities orders of magnitude greater than water (table 1) [22], perhaps explaining the general reluctance to pursue high-resolution imaging in viscous environments. By understanding how viscosity impacts upon both the thermal noise and the measured signal (and therefore SNR), key parameters can be identified which may be tuned to optimize imaging in low Q environments and extend routine high-resolution AFM to operation in high viscosity fluids. Additionally, a reduction in Q has the added benefit of increasing the mechanical bandwidth of the cantilever, which may facilitate high-speed imaging [23].

The dynamic motion of a cantilever is affected by both the density and viscosity of its environment [24, 25]. For a cantilever in a liquid environment, this results in a reduction of the resonant frequency and a decrease in Q compared to operation in air or UHV. For AFM experiments with negligible detection noise, the performance of the measurement is determined by the SNR due to the thermo-mechanical motion (i.e., the thermal noise) of the cantilever. For frequency modulation AFM (FM-AFM) the minimum detectable force gradient, F'_{min}, due to the thermal noise limit is given by [26]:

$$F'_{min} = \sqrt{\frac{2k_n k_B T B}{\pi f_n Q_n A_n^2}} \qquad (1)$$

where, $k_B T$ is the thermal energy, B is the detection bandwidth, k_n is the spring constant, f_n is the resonance frequency, A_n is the driven amplitude and Q_n is the intrinsic Q of the nth eigenmode over the ground frequency f_0, measured from a thermal noise spectrum. This is in contrast to the *driven Q, Q_D*, which is defined by the slope of the phase versus frequency curve for an actuated cantilever. Equation 1 has been experimentally verified in numerous FM-AFM [27-30] and micromechanical cantilever sensor studies [31-33]. Originally derived for UHV experiments, it incorporates two assumptions: i) $Q_D = Q_n$, and ii) B is far greater than the cantilever bandwidth, $B_{cant} = f_n/2Q_n$ ($B \gg B_{cant}$) [34]. Under these conditions, equation 1 predicts an increase of F'_{min} with decreasing Q, implying that operation in high viscosity environments results in reduced performance (i.e., lower SNR) for the same force gradient [14, 29]. However, in liquid environments both assumptions may be violated by i) non-ideal cantilever actuation [35-38] resulting in $Q_D \neq Q_n$, and ii) a lowering of Q_n resulting in $B < B_{cant}$.

In this paper, we investigate the noise contribution due to the thermal motion of the cantilever theoretically and provide experimental evidence of high SNR operation in a low Q environment. Recently, several authors have presented noise calculations that focused on frequency noise in FM-AFM [29, 30, 39, 40]. Here, we investigate the thermal noise limited performance of all dynamic AFM modes by deriving expressions for the measured amplitude noise, $\langle \delta A \rangle$, phase noise, $\langle \delta \varphi \rangle$, frequency noise, $\langle \delta f \rangle$, minimum detectable force, F_{min}, and force gradient F'_{min}, arising due to the thermal motion of the cantilever under both low Q ($B \ll B_{cant}$) and high Q ($B \gg B_{cant}$) approximations (See Section 2.1). The resulting expressions predict that under certain low Q conditions (low Q_n and $Q_D \gg Q_n$) the measured noise in FM-AFM may be further reduced by increasing the viscosity, in apparent contradiction with the implications of equation 1. We show later that this discrepancy may be reconciled by the reduced sensitivity of the frequency shift signal to force gradients.

The implications of this noise reduction for different dynamic AFM modes, namely amplitude modulation (AM), phase modulation (PM) and FM-AFM, are discussed. We then investigate and verify that the measured noise is comparable to the predictions of our theory. We further demonstrate that both AM and FM operation in a high viscosity fluid permits commensurate atomic resolution imaging of highly ordered pyrolytic graphite (HOPG) and mica surfaces with high SNR. We go on to show that the measured noise levels are in good agreement with our theory and discuss our experiments in the context of SNR and tip-sample interaction forces in high viscosity environments. Finally, we identify the parameter space where the thermal noise contribution is minimized, and make general recommendations for how to maximize SNR.

2. Theoretical considerations

In the absence of detection noise, the thermal noise of the cantilever will limit the smallest detectable signal and thus define the performance limit (SNR $= \frac{\text{Signal}}{\text{Noise}} > 1$) for a given experiment. Therefore, the amplitude, phase and frequency noise will limit AM, PM and FM operation, respectively.

2.1 Noise calculations for AM and PM

The amplitude response function, $G(f)$, of an AFM cantilever to an external driving force, $F_{drive}(f)$, can be approximated as the response of a simple harmonic oscillator (SHO) [41]:

$$G(f) = \frac{A(f)}{A_{drive}(f)} = \frac{1}{4\pi^2 \, m^* \sqrt{(f_n^2 - f^2)^2 + \left(\frac{f f_n}{Q_n}\right)^2}} \qquad (2)$$

In liquid environments, the increased viscous damping and the higher density of the fluid around the cantilever has two effects: (*i*) an increased energy dissipation, which lowers Q_n, and (*ii*) an increased effective mass, m^*, due to coupling of the surrounding fluid to the motion of the cantilever, thereby reducing f_n [25]. These changes in the mechanical response directly impact the spectral distribution of the thermal noise of the cantilever sensor.

The spectral noise density, $N_{th}(f)$, of a SHO subject to thermal fluctuations, $F_{th}(f)$, can be described by [29] (see also Appendix A):

$$N_{th}(f) = F_{th}(f)G(f) = \sqrt{\frac{2k_BT}{\pi Q_n k_n f_n \left[\left(1 - \left(\frac{f^2}{f_n^2}\right)\right)^2 + \left(\frac{f}{f_n Q_n}\right)^2\right]}} \qquad (3)$$

Frequency spectra for a typical AFM cantilever (k_0 = 40 N/m, f_0 = 100 kHz) according to equation 3 for a range of Q_0 values are shown in figure 1. For the following discussion, we define the modulation frequency, f_m, of a signal at frequency f close to f_n as $f_m = f - f_n$. As demonstrated in figure 1(b), the spectral noise density is approximately constant within B_{cant}, i.e., for frequencies $f_m < B_{cant}/2 = f_n/(4Q_n)$, thus:

$$N_{th}(f_m) \approx \sqrt{\frac{2k_BTQ_n}{\pi k_n f_n}} \qquad (4)$$

For frequencies $f_m \gg B_{cant}/2$, equation 3 can be approximated by [29]:

$$N_{th}(f_m) \approx \sqrt{\frac{k_BT f_n}{2\pi k_n Q_n}} \frac{1}{f_m} \qquad (5)$$

To distinguish between the two approximations, we can define a critical Q value, $Q_C = f_n/2B$. For a given system comprising a cantilever (characterized by Q_n) and detection system (characterized by B).

we define a low Q system as $Q_n < Q_C$ and a high Q system as $Q_n \gg Q_C$. In a UHV environment the cantilever can be regarded has a high Q system, whereas in most liquids the cantilever can be regarded as a low Q system.

In addition to the thermal noise, the detection system will generally add a constant noise density, N_{DS}. Taking this into account and using the low Q approximation (equation 4), the $\langle \delta A \rangle$ within B can be written as [14]:

$$\langle \delta A \rangle = \sqrt{\int_{-B/2}^{B/2} [N_{th}^2(f_m) + N_{DS}^2] \, df_m}$$

$$\langle \delta A_{lowQ} \rangle = \sqrt{\left(\frac{2 k_B T Q_n}{\pi k_n f_n} + N_{DS}^2\right) B} \qquad (6)$$

where the angular brackets indicate integration over the detection bandwidth. In the case of a high Q system, we assume that all the thermal energy for a given eigenmode ($\frac{1}{2} k_B T$) is contained within B. Thus, the amplitude noise becomes [230, 42]:

$$\langle \delta A_{highQ} \rangle = \sqrt{\frac{k_B T}{k_n} + N_{DS}^2 B}. \qquad (7)$$

The approximated $\langle \delta A \rangle$ defines the lower amplitude limit for AM experiments (here SNR $= A/\langle \delta A \rangle$). We observe that $\langle \delta A_{highQ} \rangle$ is dependent on k_n whereas $\langle \delta A_{lowQ} \rangle$ is dependent upon k_n, f_n and Q_n. $\langle \delta A_{lowQ} \rangle$ may therefore be reduced by using stiffer cantilevers or higher vibrational eigenmodes ($n > 0$) [43], but such effects may be attenuated by a corresponding increase in Q. Small cantilevers, with increased resonance frequencies without a corresponding increase in spring constant or Q_n [44] may yield increased performance relative to conventional cantilevers. In low Q environments, we observe that $\langle \delta A \rangle$ may be reduced by further lowering Q_n by increasing the viscosity of the environment (lower limit $Q_n \gtrsim 1$), thereby facilitating experiments at small amplitudes [14, 28].

In a driven system, the amplitude noise density, $N_{th} + N_{DS}$, will couple into the phase of a carrier signal at the nth resonance frequency f_n with amplitude, A_n (see Ref. [45] for an illustration). The spectral phase noise density, $\delta \varphi$, on this carrier signal due to a weak amplitude noise source at f_m is approximated by:

$$\delta \varphi \approx \frac{N_{th}(f_m) + N_{DS}}{A_n} \qquad (8)$$

Using the low Q approximation (equation 4), the phase noise, $\langle \delta \varphi \rangle$, becomes [46]:

$$\langle \delta \varphi \rangle = \sqrt{\int_{-B/2}^{B/2} [\delta \varphi(f_m)]^2 df_m}$$

$$\langle \delta\varphi_{lowQ} \rangle = \frac{1}{A_n} \sqrt{\left(\frac{2k_B T Q_n}{\pi k_n f_n} + N_{DS}^2 \right) B} \quad (9)$$

For the high Q approximation (equation 5) $\langle \delta\varphi \rangle$ becomes:

$$\langle \delta\varphi_{highQ} \rangle = \frac{1}{A_n} \sqrt{\frac{k_B T}{k_n} + N_{DS}^2 B} \quad (10)$$

For AM operation in a high Q environment, the fundamental noise limits for both amplitude and phase signals are independent of Q_n (equations 7 and 10). In the low Q regime, the SNR for both AM and PM-AFM can be increased by decreasing Q_n (lower limit $Q_n \gtrsim 1$).

2.2 Noise calculations for FM

In FM, a frequency shift, Δf, of the resonance frequency of the cantilever occurs due to the presence of a force gradient, $F' = \partial F/\partial z$. In the case of a small oscillation amplitude, the following approximation can be used [26]:

$$F' = \frac{2k_n \Delta f}{f_n} \quad (11)$$

where Δf is measured via either a self-excitation [26] or by employing a feedback loop [47]. In both cases, two contributions to the observed frequency noise are present: i) frequency fluctuations in the carrier signal caused by amplitude noise close to the drive frequency, termed *intrinsic frequency noise*, $\langle \delta f^I \rangle$, and ii) noise due to the conversion of phase fluctuations into frequency fluctuations, termed *phase transfer noise*, $\langle \delta f^{PT} \rangle$. The total observed frequency noise will be the sum of these two contributions. Here, we derive expressions for and discuss the relevance of both of these noise contributions.

2.2.1 Intrinsic frequency noise

The amplitude noise at a sideband f_m will couple into the carrier signal at f_n and modulate its frequency for $|f_m| < B/2$. Following the approach of Kobayashi *et al.*, we find for frequency fluctuations in the carrier signal [29]:

$$\delta f = \delta\varphi \, f_m = \frac{N_{th}(f_m) + N_{DS}}{A_n} f_m \quad (12)$$

The total intrinsic frequency noise, $\langle \delta f^I \rangle$, can then be obtained by integrating over B:

$$\langle \delta f^I \rangle = \sqrt{\int_{-B/2}^{B/2} [\delta f(f_m)]^2 df_m}$$

$$\langle \delta f^I_{lowQ} \rangle = \frac{1}{2A_n} \sqrt{\left(\frac{2k_BTQ_n}{\pi k_n f_n} + N^2_{DS}\right)\frac{B^3}{3}} \quad (13)$$

For high Q systems, we can use equation 5 to approximate $N_{th}(f_m)$:

$$\langle \delta f^I_{highQ} \rangle = \frac{1}{A_n} \sqrt{\frac{k_BTf_n}{2\pi k_n Q_n}B + \frac{N^2_{DS}}{12}B^3} \quad (14)$$

In the absence of detection noise F'_{min}, derived from the high Q approximation (equations 11 and 14), is consistent with the well-known results from Albrecht *et al.* (see equation 1 and Appendix B) [26]. In contrast, the low Q approximation predicts decreased intrinsic frequency noise when $1 < Q_n \ll Q_C$. Note that the low Q approximation for $\langle \delta f^I \rangle$ scales as $\sqrt{Q_n}$ whereas the high Q approximation scales as $1/\sqrt{Q_n}$.

2.2.2 Phase transfer noise

When implementing FM-AFM by means of a self-oscillation loop, the deflection signal is amplified and phase shifted before being used to drive the cantilever [26]. In the feedback implementation of FM-AFM, the frequency shift is detected by a frequency feedback loop which monitors φ and adjusts f in order to maintain $\varphi = 90°$ [47]. In both cases, a Δf due to, e.g., tip-sample interactions leads to a phase shift, $\Delta\varphi$:

$$\Delta f = \left|\frac{d\varphi}{df}\right|^{-1}\Delta\varphi \quad (15)$$

where the inverse phase slope, $|d\varphi/df|^{-1}$, is the sensitivity of the frequency detection system. In a driven SHO, the phase slope at f_n is:

$$\left.\frac{d\varphi}{df}\right|_{f=f_n} = \frac{2Q_D}{f_n} \quad (16)$$

The actuation of cantilevers in low Q environments can result in $Q_D \gg Q_n$ due to resonance coupling and a non-ideal actuator transfer function [35-38]. Under these conditions, the measured frequency shift, $\Delta f_{measured}$, required to compensate $\Delta\varphi$ is reduced by Q_D/Q_n (see Ref [39] for an illustration):

$$\Delta f = \frac{Q_D}{Q_n}\Delta f_{measured} \quad (17)$$

The FM detection system propagates phase fluctuations, $\langle \delta\varphi \rangle$, into the frequency signal according to equation 15 [29]. As a result [39], the frequency noise due to phase fluctuations, i.e., the phase transfer noise, $\langle \delta f^{PT} \rangle$, is also reduced:

$$\langle \delta f^{PT} \rangle = \frac{f_n}{2Q_D} \langle \delta\varphi \rangle \qquad (18)$$

Using the low and high Q approximations (equations 9 and 10) equation 18 becomes:

$$\langle \delta f_{lowQ}^{PT} \rangle = \frac{f_n}{2Q_D A_n} \sqrt{\left(\frac{2k_B T Q_n}{\pi k_n f_n} + N_{DS}^2 \right) B} \qquad (19)$$

$$\langle \delta f_{highQ}^{PT} \rangle = \frac{f_n}{2Q_D A_n} \sqrt{\frac{k_B T}{k_n} + N_{DS}^2 B} \qquad (20)$$

Note that $\langle \delta f_{highQ}^{PT} \rangle$ is dependent on Q_D whereas $\langle \delta f_{lowQ}^{PT} \rangle$ depends on both Q_D and Q_n.

The total frequency noise, $\langle \delta f^{total} \rangle$, is then the sum $\langle \delta f^I \rangle$ and $\langle \delta f^{PT} \rangle$, i.e., $\langle \delta f^{total} \rangle = \langle \delta f^I \rangle + \langle \delta f^{PT} \rangle$. For the case of identical driven and intrinsic Q ($Q_D = Q_n$) we find that $\langle \delta f_{lowQ}^I \rangle < \langle \delta f_{lowQ}^{PT} \rangle$ and $\langle \delta f_{highQ}^I \rangle > \langle \delta f_{highQ}^{PT} \rangle$ (see Appendix B for a formal proof). In the low Q regime, $Q_D > Q_n$ yields lower $\langle \delta f_{lowQ}^{PT} \rangle$ resulting in a reduction in measured frequency noise for FM-AFM (here, SNR = $\Delta f / \langle \delta f^{total} \rangle$). Interestingly, in the absence of instrument noise, setting $Q_D = Q_n$ in equation 19 yields an identical expression to the intrinsic frequency noise for high Q environments (equation 14) [29]. Thus, if $Q_D \not> Q_n$ for the driven system, $\langle \delta f^{total} \rangle$ will increase in low Q environments. Since the same scaling (equation 17) applies to both the signal and the noise, any reduction in the measured frequency noise due to $Q_D > Q_n$ will not result in enhanced SNR.

2.3 Approximations vs. simulations

In order to compare the low and high Q approximations with exact numerical data and thus define conditions under which they are valid, AM noise values, $\langle \delta A \rangle$ and $\langle \delta \varphi \rangle$, and FM intrinsic frequency noise values, $\langle \delta f^I \rangle$, were plotted as a function of Q_n / Q_C (figure 2). For these simulations, we used values for a typical high-resolution experiment in water (k_0 = 40 N/m, f_0 = 100 kHz, B = 1 kHz, A_0 = 1 nm [15, 16]; $Q_C = 50$). Exact values were obtained by numerically integrating equation 3 over B. The solid black curves in figure 2 and figure 3 correspond to exact numerical data, whereas the blue and red curves correspond to low and high Q approximations, respectively.

2.3.1. AM and PM noise

The dependence of $\langle \delta A \rangle$ and $\langle \delta \varphi \rangle$ upon Q are shown in figure 2a. For $Q_n \gg Q_C$ the total thermal noise of the eigenmode is contained within B and thus is independent of Q. The exact solution (thick black curve) yields lower values than predicted by the high Q approximation (red line) for $Q_n \lesssim Q_C$, merging with the $1/\sqrt{Q_n}$ slope of the low Q approximation (blue line) for $Q_n < Q_C$. Figure 2a demonstrates that the respective approximations for low and high Q environments are well suited to

describe the amplitude and phase noise and that the fundamental limit of imaging performance can be directly influenced by the choice of imaging environment.

2.3.2 Intrinsic frequency noise

Figure 2(b) shows the Q dependence of $\langle \delta f^{I} \rangle$ where the exact solution shows a maximum at $Q_n/Q_C \approx$ 3. At $Q_n/Q_C = 1$, the deviation between the approximations and exact solution is $< 10\%$ and $\sim 270\%$ for the low Q and high Q approximations, respectively. A deviation of less than 2 % can be achieved for $Q_n/Q_C > 100$ for the high Q approximation and $Q_n/Q_C < 0.5$ the low Q approximation.

2.3.3 Total frequency noise

Figure 3 shows $\langle \delta f^{total} \rangle$, F'_{min} and F_{min} as a function of Q_n/Q_C. Here, the solid black curves correspond to exact numerical data, whereas the blue curves in (a) and (b) and the red curves in (c) and (d) correspond to the low and high Q approximations, respectively. In order to demonstrate the influence of driven Q enhancement ($Q_D > Q_n$) we also include solutions for $Q_D = 10 \times Q_n$ and $Q_D = 100 \times Q_n$ (dashed lines). The shading in figure 3 indicates regions where the approximations deviate by $< 10\%$ from the exact solutions for the low Q ((a) and b)) and high Q approximations ((a) and b)), respectively. The most striking result is that the effect of $Q_D > Q_n$ on the measured frequency noise is much stronger in the low Q regime. In the high Q regime, the influence of $Q_D > Q_n$ is negligible as $\langle \delta f^{I} \rangle$ dominates. For $Q_D = Q_n$, $\langle \delta f^{PT} \rangle$ dominates for $Q_n/Q_C < 10$ resulting in $\langle \delta f^{total} \rangle$ increasing with decreasing Q_n, even below Q_C. The influence of $\langle \delta f^{PT} \rangle$ in low Q environments may be reduced by utilizing $Q_D > Q_n$ via piezo actuation or employing actuation techniques such as Q control. Moderate enhancement of Q_D with respect to Q_n can result in significant reduction in the measured $\langle \delta f^{total} \rangle$ in low Q environments. For $Q_D = 100 \times Q_n$, $\langle \delta f^{total} \rangle$, becomes limited by the intrinsic noise of the cantilever in the range of $0.1 > Q_n/Q_C < 1$. However, this noise reduction is accompanied by a reduced sensitivity of Δf to a given F', resulting in F_{min} and F'_{min} increasing monotonically as Q_n decreases (Figure 3 (b) and (d)).

3. Materials and methods

In order to test the predictions of improved SNR in low Q environments, we performed thermal noise limited imaging experiments on a low-noise AFM system in a viscous environment.

3.1 Instrumentation

A bespoke low-noise AFM system described in detail elsewhere [11] was used for all measurements. Two different cantilevers were used, which we will refer to as SCD-cantilever and Si-cantilever, respectively. The SCD-cantilever is a silicon cantilever a with a single crystalline diamond (SCD) tip glued to its end (DP15/SCD by MikroMasch). The Si-cantilever is a NCH-SSS cantilever

(Nanosensors) with a resonant frequency of 330 kHz and a force constant of 42 N/m (nominal values) – a commonly used cantilever for high-resolution studies in liquid [15, 16]. In all experiments we used $B = 1$ kHz. In order to further improve the noise performance, the experiments were performed on the second eigenmode which increases both k_n and f_n [43]. FM-AFM was performed at constant amplitude, i.e., an additional feedback loop was employed to keep the cantilever amplitude constant. Experiments were performed in a mixture of glycerol ($\geq$ 99.5%, Sigma Aldrich, CAS: 56-81-5) and water (Millipore, Gradient A10). Such mixtures have the advantage of allowing the viscosity of the liquid to be tuned over a wide range from 1 mPa·s (pure water) to 1.4 Pa·s (pure glycerol) by changing the mixing ratio [48]. A mixture of 70% by volume of glycerol with a calculated viscosity of ~ 33 mPa·s at 21°C was found to satisfy $1 < Q_n \ll Q_C$ for both cantilevers. HOPG (Agar Scientific Ltd., G3389) and mica (SPI Supplies, 01877-MB) were used as substrates. HOPG was annealed at 120°C for 30 min prior to experiments in order to remove any organic residue. For each experiment, the freshly cleaved sample surface and cantilever were fully immersed in a droplet of 100 µL of the glycerol/water mixture and left to equilibrate overnight prior to imaging. All images were subject to 1st order flattening only and no filtering was applied. Lattice dimensions were determined using SPIP (Image Metrology A/S).

3.2 Calibration

The dynamic inverse optical lever sensitivity (InvOLS) was determined in air using a combination of the Sader *et al*. [49] and Higgins *et al*. [50] methods and the plan view dimensions of the SCD cantilever determined from scanning electron microscope images (not shown). The spring constant of the fundamental resonant mode was then determined by the thermal method in air [49]. We use a factor of 40.2 to scale the fundamental spring constant, k_0, measured in air to determine the spring constant of the second resonant mode ($k_1 = 40.2 \times k_0$) [51]. The values for k_0 and k_1 were then assumed to be the same in the liquid environments. Using the Higgins *et al*. method allowed us to determine the dynamic InvOLS at the respective eigenmodes [50]. This dynamic InvOLS was then used to scale the thermal spectra prior to analysis (all calibration results are given in the caption of table 2). A systematic error of 20% in k_0 was used to account for any uncertainty in determining the influence of cantilever dimensions, tip position on the lever beam and its mass. This uncertainty was used in conjunction with the uncertainties in the fit parameters for the purposes of error propagation. The transfer function of the photodetector was removed from the thermal spectrum prior to scaling and analysis.

4. Results and discussion

4.1 HOPG imaging

We imaged a freshly cleaved and annealed HOPG surface with the SCD-cantilever in a 70/30 glycerol-water mixture. Figures 4 (a) and (b) show a direct comparison of height images of a HOPG surface recorded in AM and FM mode, respectively. The atomic lattice was clearly resolved, although a slight compression in one axis was observed (see figure caption). The observed contrast inversion of the honeycomb pattern is an inherent feature of non-contact AFM imaging of HOPG [52] and can be ascribed to a stronger tip-sample interaction in the centre of the hexagonal lattice (H in the section profiles of figure 4) [53]. Both AM and FM images show the occurrence of two distinct corrugation depths for different carbon lattice sites (A and B in the section profiles of figure 4), which have been observed and theoretically explained previously by considering the short-range tip-sample interactions and the structural difference between the different lattice sites [53]. Although the contrast is similar for the two images, subtle differences could be observed which are manifested as a slightly larger corrugation depth for the FM image compared to the AM image (root mean square (RMS) roughness for AM = 76 pm, FM = 82 pm). This difference can be ascribed to the different imaging mechanisms of AM and FM with the former being sensitive to the tip-sample force whilst the latter is sensitive to the force gradient. The AM signal reflects a convolution of conservative and dissipative tip-sample interactions. In FM imaging, those contributions are decoupled [14]: the frequency shift reflecting the conservative part while the dissipation (or drive) signal represents the dissipative part of the tip sample interaction [54]. In figure 5 we compare the dissipation images for AM (calculated from the measured phase and average imaging amplitude) [55] and FM (measured), which both show an increased energy dissipation of the cantilever when it is between lattice centres (H sites in figure 4).

Few groups have successfully imaged the atomic structure of graphite using dynamic AFM in liquid [56] due to the relatively weak and short range van der Waals tip-sample interactions present at the interface [52, 56-58]. Here we demonstrate that the use of a high viscosity environment can enhance the SNR to a degree that can enable imaging with true atomic resolution. In order to maximize the sensitivity of the cantilever to the short range van der Waals tip-sample interactions, amplitudes of a similar length scale must be used (here $A_1 \sim 0.6$ Å) [14, 28]. By increasing the viscosity of the imaging fluid to lower the Q of the cantilever, $\langle \delta A \rangle$ can be suppressed resulting in SNR > 100. Additionally, the role of the solvent molecules at the interface must also be considered. Since the oscillation amplitude is smaller than the glycerol molecules ($R_{solvent}$ 2.6 − 3.1 Å [59]), the solvent molecules are physically excluded from the tip-sample gap. This creates a quasi-vacuum environment, which permits the local van der Waals forces between the tip apex and the surface atoms to dominate the tip-sample interaction. Concurrently, the remainder of the tip and the cantilever experience a relatively constant background force resulting in image contrast dominated by the force variations

localized at the tip apex. This imaging mechanism is illustrated by the similarity of the line profiles (figure 4) with those obtained under low temperature UHV conditions despite the presence of fluid at the interface [53]. The use of larger oscillation amplitudes ($A_n \geq R_{solvent}$) results in not only a reduction in the local force gradient sensitivity [14, 28], but also a convolution of the solvation forces with the local tip-sample force leading to a loss of atomic resolution [17, 60]. The need for high SNR operation is exemplified by the small amplitudes required in order to obtain true atomic resolution.

4.2 Mica imaging

In order to further demonstrate true atomic resolution imaging in low Q environments is not limited to a specific tip-sample combination, a freshly cleaved mica surface was imaged with a Si-cantilever in a glycerol/water (70/30) solution. Figure 6 shows two sequentially recorded images showing a persistent atomic point defect (arrow) and a larger defect region (circled). The presence of these defects across multiple images attests to the true atomic resolution obtained under these low Q conditions. Atomic resolution imaging on mica in the glycerol/water solution is again facilitated by a combination of high SNR and using amplitudes smaller than the solvent molecules in order to enhance sensitivity to the tip-sample interactions. For this hydrophilic surface, water molecules (molecular diameter ~ 2.5 Å [61, 62]) are expected to be present at the interface. Previously, imaging with comparable amplitudes allowed for the visualization of dehydrated ions at the mica surface in aqueous solutions whereby the small oscillation amplitude excludes water from the tip-sample gap as described above [17]. Under similar conditions in viscous, ionic liquids, it may be possible to directly measure the charge distribution at the solid–liquid interface [10].

4.3 Comparison of imaging noise to theory

In order to quantify the thermal noise contributions to the SNR observed during imaging, we calculated the theoretically expected noise according to the low and high Q approximations. In order to obtain experimental values for comparison, a thermal noise spectrum was recorded close (~ 500 nm) to the surface and numerically integrated to obtain $\langle \delta A \rangle$, $\langle \delta \varphi \rangle$ and $\langle \delta f^1 \rangle$ (table 2). It was found that the low Q approximation yielded results which agreed within experimental error with the values obtained by numerical integration whilst the high Q approximation deviated by orders of magnitude. Under these conditions ($Q_1 = 2.25 \pm 0.05$, $Q_C = 442$, $B = 1$ kHz).

Additionally, we extracted the noise values from AM and FM force curves away from the surface and compared these values with the low Q and high Q approximations (Table 3). Whereas in Table 2 the intrinsic noise was evaluated, here we measure the noise for the driven system. In both cases we find that the low Q approximations are closer to the measured data than the high Q approximations. In order to stabilize the frequency feedback loop using piezo actuation, we used lower gain parameters than the ones suggested by our gain optimization algorithm [47]. Therefore, phase fluctuations are not

fully converted into frequency fluctuations, effectively lowering $\langle \delta f^{PT} \rangle$ and thus $\langle \delta f^{Total} \rangle$. This could explain why the measured frequency noise is lower than predicted by theory.

Furthermore, the observed noise may be influenced by uncertainties in determining Q_D and Q_n at the surface, resonance coupling effects (requiring operation at $f \neq f_n$) [35-37] and changes in effective viscosity as the cantilever approaches the surface [25, 63]. Alternative drive mechanisms can result in a purely SHO transfer function with $Q_D = Q_n$, e.g. photothermal [64], Lorentzian (also known as magnetic) [65] and electro-osmotic [66] excitation. Such systems, whilst having a well-defined SHO response and allowing operation at $f = f_n$, are subject to high phase transfer noise. In order to reduce the influence of the phase transfer noise, more sophisticated drive mechanisms, such as Q control, may be employed to enhance Q_D in a controlled manner [67, 68]. However, the benefits of this method with respect to SNR continue to be a topic of debate [69, 70].

In order to determine SNR in our imaging experiments (see table 3) the imaging setpoint was divided by the relevant noise parameter to obtain the measurement SNR. In the case of frequency modulation we observed a SNR of 40 which is far greater than the value of 4.6 reported previously for small cantilevers operated in an aqueous environment (setpoint 1.64 kHz, $\langle \delta f^{Total} \rangle$ = 354 Hz) [44]. The high value of 181 observed for AM imaging is consistent with the reduction in $\langle \delta A \rangle$ that occurs in low Q environments (see Figure 2a).

5. General recommendations

Our results demonstrate that thermal noise contributions are not a fundamental barrier to obtaining true atomic resolution with dynamic AFM in low Q environments. Indeed, for both AM and PM operation under low Q conditions, a ten-fold reduction in Q_n would result in a noise reduction of 68 % for $\langle \delta A \rangle$ and $\langle \delta \varphi \rangle$, enhancing SNR irrespective of the actuation mechanism. For FM operation a reduction in $\langle \delta f^{total} \rangle$ may be achieved by operating with $Q_D \gg Q_n$ but the SNR would remain unaltered. Using higher eigenmodes may also improve SNR, e.g., for the second eigenmode under low Q conditions (f_1 ~ $6.3 \times f_0$ [71], k_1 ~ $40 \times k_0$ [51], Q_1 ~ $3 \times Q_0$ [72]) the AM and PM noise is reduced by 89 % and 78 %. For FM, however, F'_{min} and F_{min} increase by 42 %. Fukuma *et al*. found that using small cantilevers in liquid with a high f_n, and low k_n and Q_n [44, 73] resulted in a reduction in F_{min} of 86.5 % [44], which agrees well with our low Q prediction of 82.4 %. Nevertheless, small cantilevers must be combined with a small laser spot size in order to achieve similar levels of instrument noise. Thus, operating in a low Q imaging environment with a higher eigenmode may be a practical method of enhancing SNR. In our case, using the second eigenmode, the SNR was 40, significantly higher than that observed in an aqueous environment [44].

For AM and PM our findings suggest that operation with the lowest Q possible ($1 < Q_n < Q_C$) and a higher eigenmode would result in the lowest noise levels. For FM, the use of small oscillation

amplitudes is facilitated in high viscosity environments by the reduction in $\langle\delta A\rangle$ which increases sensitivity to local force gradients and enhances lateral resolution [14, 28]. A decrease in sensitivity to local force fields in low Q environment may require operating at higher imaging forces. The presence of less mobile liquid molecules close to the surface is likely to enhance the local force fields, thereby explaining the high SNR values we observed. Additionally, operation in low Q environments increases the mechanical bandwidth of the cantilever (here $B_{cant}^{air} \sim 2.5$ kHz compared to $B_{cant}^{liquid} \sim 200$ kHz), creating a significant opportunity to investigate such systems at high speed with true atomic resolution without needing to resort to small cantilevers [23].

6. Conclusions

We have developed a theoretical description of the thermal noise limits of dynamic AFM. The low Q approximations were found to agree with measured values within 1.5% for $\langle\delta A\rangle$ and $\langle\delta\varphi\rangle$, and within 4% for $\langle\delta f^I\rangle$, respectively. Furthermore, we demonstrated that despite the decreased sensitivity of FM-AFM to local force fields, imaging under low Q conditions can yield true atomic resolution imaging for both hydrophobic and hydrophilic surfaces in both AM and FM modes. Images of a HOPG surface obtained under these conditions with AM and FM-AFM were consistent with those obtained under low-temperature UHV conditions [52]. The difference between A and B carbon sites in the carbon hexagon structure could be readily observed – a structure that so far has only been observed under UHV conditions. The observation of high SNR values suggests that the strength of the force field is likely increased due to the presence of less mobile liquid molecules close to the surface, yielding a larger signal. Understanding the exact nature of such solid–liquid interactions and the mechanism by which they apparently give rise to high force fields in low Q environments has the potential to provide fundamental insights into the physics of the solid-liquid interface in viscous environments. This will be the subject of further investigations.

Having demonstrated the agreement between theory and experimental noise contributions, we then outlined a set of recommended operating conditions where optimal SNR may be achieved. We therefore conclude that high viscosity environments are not an intrinsic obstacle for true atomic resolution imaging and spectroscopy of solid–liquid interfaces. This new understanding of the influence of the imaging environment on the noise contributions serves as a basis for widening the scope of high-resolution AFM away from water based applications to a wide variety of energy related materials, ionic and organic liquids. This is a fundamental shift in the field which will lead to a greater understanding of a range of processes at the solid–liquid interface, e.g., ionic transport and energy storage, which will be essential for improving the performance of energy storage devices. The increased mechanical bandwidth of the cantilever in low Q environments also represents an opportunity to not only exploit this high-resolution operation but to do so at high speed, and thus study the temporal evolution of these phenomena at the solid–liquid interface.

Acknowledgements

Appendices

Appendix A: Thermal forces

In an oscillator connected to a heat bath of temperature T, thermal fluctuations in the nth eigenmode will have an energy of $\frac{1}{2} k_B T$:

$$E_{th} = \frac{1}{2} k_n < z^2 > = \frac{1}{2} k_B T \qquad (A.1)$$

where $< z^2 >$ is the average deflection of the cantilever, which can also be written in the form

$$< z^2 > = \int_0^\infty F_{th}^2(f) \, |G(f)|^2 df \qquad (A.2)$$

where F_{th} is the thermal noise force density. The thermal force is a white noise and thus independent of f. With this assumption and by solving the integral in equation A.2, we find:

$$F_{th} = \sqrt{\frac{2 k_B T k_n}{\pi Q_n f_n}} \qquad (A.3)$$

This thermal force spectral density (unit: $N/\sqrt{Hz}$) is the mechanical force acting on the cantilever due to Brownian motion in the surrounding medium. With increasing viscosity in the medium, the dissipation increases and Q_n decreases. Thus, the thermal force acting on the cantilever increases. In high Q environments the thermal force becomes weak. Nevertheless, the total energy in the thermal motion remains $\frac{1}{2} k_B T$. In high Q environments, where $B \gg B_{cant}$, all of the energy is contained with B. In low Q environments, where $B \ll B_{cant}$, only a small portion of the energy may be contained within B.

Appendix B: Limits of force and force gradient detection

The complete expression for the measured frequency noise $\langle \delta f^{total} \rangle$ is given by:

$$\langle \delta f^{total} \rangle = \langle \delta f^{I} \rangle + \langle \delta f^{PT} \rangle \qquad (B.1)$$

$$\langle \delta f^{total}_{lowQ} \rangle = \frac{1}{2A_n} \sqrt{\left(\frac{2k_B T Q_n}{\pi k_n f_n} + N_{DS}^2 \right) \frac{B^3}{3}} + \frac{f_n}{2Q_D A_n} \sqrt{\left(\frac{2k_B T Q_n}{\pi k_n f_n} + N_{DS}^2 \right) B} \qquad (B.2)$$

$$\langle \delta f^{total}_{highQ} \rangle = \frac{1}{A_n} \sqrt{\frac{k_B T f_n}{2\pi k_n Q_n} B + \frac{N_{DS}^2}{12} B^3} + \frac{f_n}{2Q_D A_n} \sqrt{\frac{k_B T}{k_n} + N_{DS}^2 B} \qquad (B.3)$$

We discussed in section 2.3 that $\langle \delta f^{I} \rangle$ dominates $\langle \delta f^{total} \rangle$ in the high Q regime. A more formal proof of this finding can be obtained by solving the following inequality for high Q:

$$\langle \delta f^{I} \rangle > \langle \delta f^{PT} \rangle \qquad (B.4)$$

$$\frac{1}{A_n} \sqrt{\frac{k_B T f_n}{2\pi k_n Q_n} B + \frac{N_{DS}^2}{12} B^3} > \frac{f_n}{2Q_D A_n} \sqrt{\frac{k_B T}{k_n} + N_{DS}^2 B}$$

In the absence of instrument noise ($N_{DS} = 0$) and using $Q_n = Q_D$ we get:

$$Q_n > \frac{f_n}{2B} \equiv Q_C \quad (B.5)$$

This equation is exactly the definition for a high Q system in section 2.1. Therefore, it is justified to ignore $\langle \delta f^{PT} \rangle$ in the high Q regime at $Q_n \gg Q_C$.

In the low Q regime, the dominating noise term strongly depends on the value of Q_D. By introducing the Q enhancement factor

$$\kappa = \frac{Q_D}{Q_n} \qquad (B.6)$$

and solving the inequality in (B.4) for low Q, we get

$$\frac{1}{2A_n} \sqrt{\left(\frac{2k_B T Q_n}{\pi k_n f_n} + N_{DS}^2 \right) \frac{B^3}{3}} > \frac{f_n}{2\kappa Q_n A_n} \sqrt{\left(\frac{2k_B T Q_n}{\pi k_n f_n} + N_{DS}^2 \right) B}$$

$$\kappa > \frac{\sqrt{3} f_n}{B Q_n} \equiv 2\sqrt{3} \frac{Q_C}{Q_n} \qquad (B.7)$$

Therefore, $\langle \delta f^{total}_{lowQ} \rangle$ will be dominated by $\langle \delta f^{I} \rangle$ if $\kappa > 2\sqrt{3} \frac{Q_C}{Q_n}$. For lower Q_n that means that a larger κ will be required in order for the system to be limited by $\langle \delta f^{I} \rangle$. Another implication of equation B.7 is that if $\kappa = 1$ (i.e., $Q_D = Q_n$), $\langle \delta f^{PT} \rangle > \langle \delta f^{I} \rangle$ throughout the low Q regime.

If equation (B.7) is fulfilled, the intrinsic low Q approximations predict decreased noise for FM-AFM when $1 < Q_n \ll Q_C$. Note that the low Q approximations all scale as $\sqrt{Q_n}$ whereas the high Q approximations scale as $1/\sqrt{Q_n}$.

In order to obtain the limits of force detection for FM-AFM, we have to consider the relationship between $\Delta f_{measured}$ and F'_{min}. We have shown in section 2.2.2 that in the case of $Q_D \neq Q_n$, the measured frequency shift has to be corrected according to equation 17 to obtain the real frequency shift of the underlying SHO [39]. From the corrected frequency shift, the force gradient experienced by the tip can be calculated via equation 11.

In a low Q environment, the frequency noise is generally dominated by phase transfer noise, in particular when Q_n is very low and when no or moderate Q enhancement is being applied. Under these conditions we get for the minimum detectible force gradient:

$$F'^{min}_{lowQ} \approx \sqrt{\frac{2k_BTk_nB}{\pi f_nQ_nA_n^2} + \left(\frac{k_nN_{DS}}{f_nQ_nA_n}\right)^2 B} \qquad \text{(B.8)}$$

For high Q systems, $Q_D \approx Q_n$ and we can thus assume that the intrinsic frequency noise dominates. Thus we get:

$$F'^{min}_{highQ} \approx \sqrt{\frac{2k_BTk_nB}{\pi f_nQ_nA_n^2} + \left(\frac{k_nN_{DS}}{f_nA_n}\right)^2 \frac{B^3}{3}} \qquad \text{(B.9)}$$

In the absence of detection noise ($N_{DS} = 0$), both expressions are equivalent and identical to equation 1. In the limit of small amplitudes, F_{min} can be approximated by assuming a constant force gradient over $2A_n$:

$$F_{min} \approx F'_{min} \, 2A_n = \frac{4A_nk_n\langle\delta f\rangle}{f_n} \qquad \text{(B.10)}$$

For F_{min} we obtain the following low and high Q approximations:

$$F^{min}_{lowQ} = \sqrt{\frac{8k_BTk_nB}{\pi f_nQ_n} + \left(\frac{2k_nN_{DS}}{f_nQ_n}\right)^2 B} \qquad \text{(B.11)}$$

$$F^{min}_{highQ} = \sqrt{\frac{8k_BTk_nB}{\pi f_nQ_n} + \left(\frac{2k_nN_{DS}}{f_n}\right)^2 \frac{B^3}{3}} \qquad \text{(B.12)}$$

TABLES

Table 1. Room temperature viscosities (values taken from [22, 48]) of imaging media used in the AFM studies referenced in the third column. BMIN PF_6 refers to the ionic liquid of 1-Butyl-3-methylimidazolium hexafluorophosphate.

Liquid	Viscosity [mPa·s]	Ref.
Water	1	
Decane	0.92	[1]
Decanol	12	[3]
Dodecane	1.5	[2]
Decalin	2.5	[2]
Squalene	30	[2]
BMIN PF_6	312	[5]
Glycerol/water (70/30)	35.3	

Table 2. Comparison of experimental and theoretical noise values. The experimental parameters were: $f_1 = 884 \pm 3$ kHz, $k_1 = 1779 \pm 451$ N/m, $Q_1 = 2.25 \pm 0.05$, $Q_C = 442$, $B = 1$ kHz. The noise values were obtained by numerically integrating the measured thermal noise spectrum.

	Integrated Noise	Intrinsic Low Q	% Deviation	High Q Theory	% Deviation
AM Imaging:					
$\langle \delta A \rangle$ [pm]	0.166 ± 0.022	0.164 ± 0.003	1.5	1.53 ± 0.19	819
$\langle \delta \varphi \rangle$ [deg]	0.142 ± 0.018	0.140 ± 0.003	1.5	1.31 ± 0.16	819
FM Imaging:					
$\langle \delta f^1 \rangle$ [Hz]	0.82 ± 0.11	0.785 ± 0.014	4.1	200 ± 25	24300

Table 3. Comparison of experimental noise obtained from force curves with theoretical noise values. The experimental parameters were the same as given in the caption of Table 2. The AM force curve was collected with an amplitude of 299.3 ± 0.5 pm. The imaging SNR is the imaging setpoint (AM: $\Delta A_1 = 67$ pm, FM: $\Delta f_1 = 110$ Hz and $A_1 = 60$ pm) divided by the measured noise from the force curves.

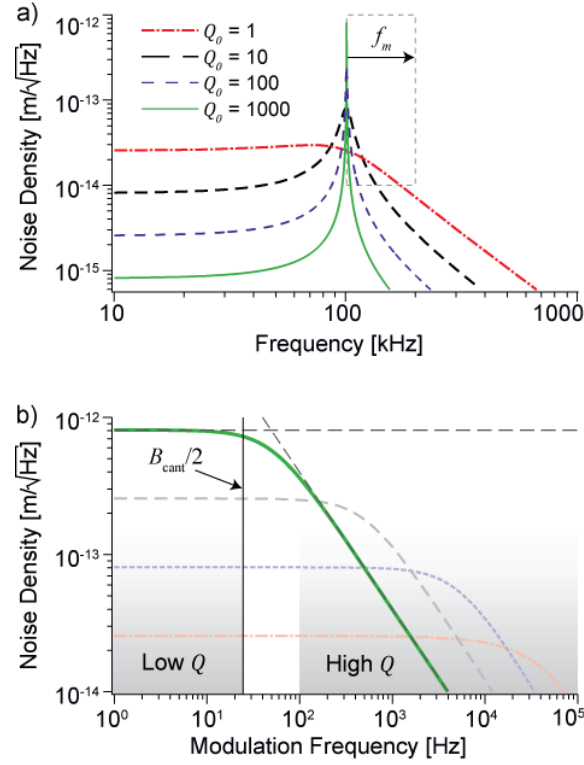|	Measured Noise	Low Q Theory	High Q Theory	Imaging SNR
AM Imaging:				
$\langle \delta A \rangle$ [pm]	0.37	0.164 ± 0.003	1.53 ± 0.19	181
$\langle \delta \varphi \rangle$ [deg]	0.032	0.0314 ± 0.0006	0.0318 ± 0.0041	–
FM Imaging:				
$\langle \delta f^{Total} \rangle$ [Hz]	2.75	10.23 ± 0.20	287.93 ± 27.76	40

FIGURES

Figure 1. a) Calculated spectral thermal noise density for a SHO according to equation 3 (f_0 = 100 kHz, k_0 = 40 N/m for Q_0 values between 1 and 1000). b) Logarithmic plot of the same data in the region around the resonance frequency (marked by a dashed box in a)) as a function of modulation frequency ($f_m = f - f_0$). The case for Q_0 = 1000 is highlighted (green). For detection bandwidths smaller than the cantilever bandwidth (vertical line) the noise density is approximately constant and can be approximated by equation 4. For detection bandwidths much larger than B_{cant} the noise density merges with the $1/f$ approximation of equation 5.
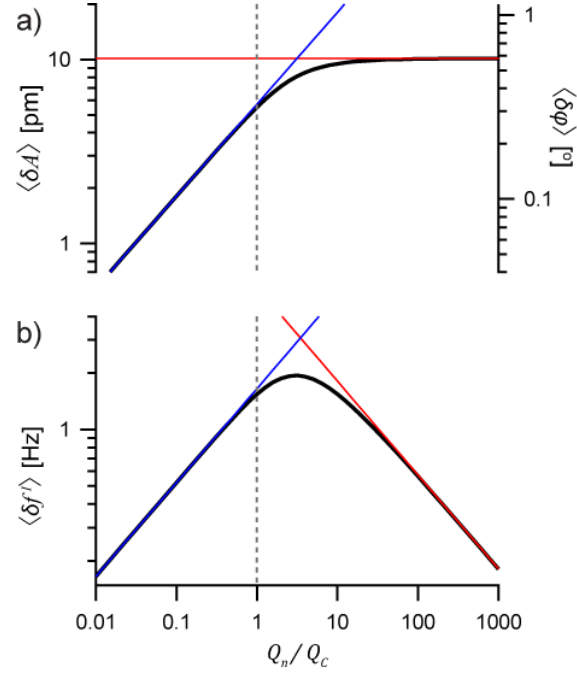
Figure 2. Comparison of the numerically integrated (thick black curve) a) amplitude, phase and b) $\langle \delta f^I \rangle$ to both the low Q (blue line) and high Q (red line) approximations as a function of Q_n/Q_C ($f_0 = 100$ kHz and $k_0 = 40$ N/m, $A_0 = 1$ nm, $B = 1$ kHz, $Q_c = 50$).
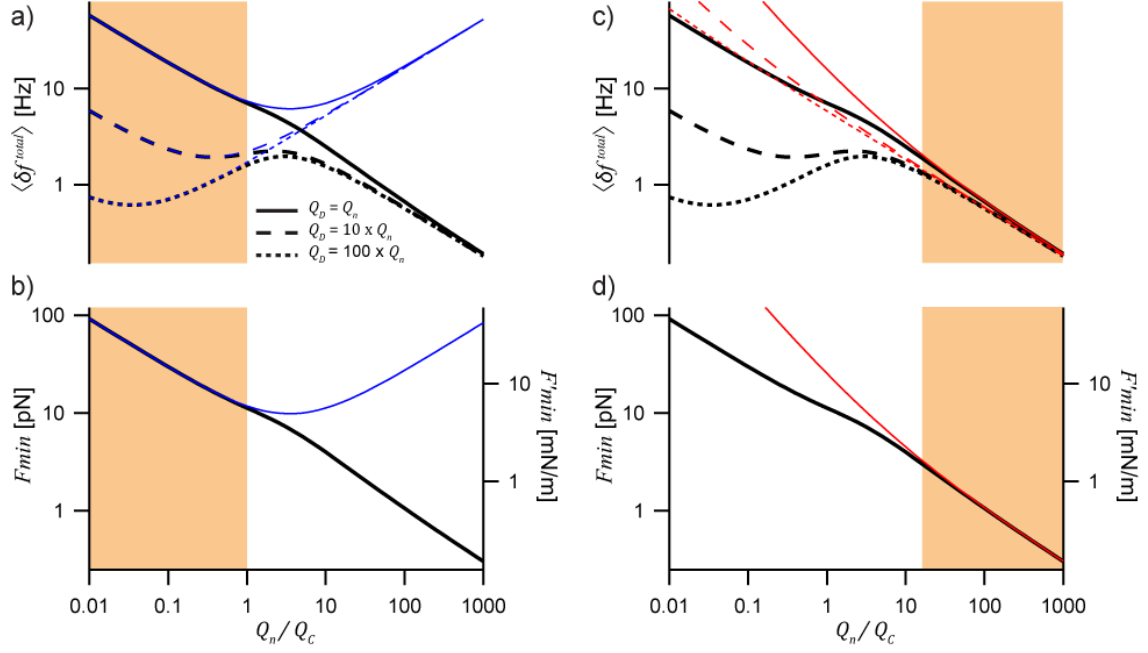
Figure 3. Low Q (blue thin curve in (a) and (b)) and high Q (red thin curves in (c) and (d)) approximations for $\langle \delta f^{total} \rangle$ ((a) and (c)) and F'_{min} and F_{min} ((b) and (d)). The thick black curves are exact solutions from numerical integration. The effect of enhancement of the driven Q_D is demonstrated by the dashed curves in a) and c). In particular in the low Q regime (shaded area in a) and b)), Q enhancement can suppress noise. In the high Q regime (shaded area in c) and d)), Q enhancement only has a limited effect on the frequency noise. The data is plotted as a function of Q_n/Q_C ($Q_C = 50$). Shading indicates regions where the approximations deviate from the exact solutions by $< 10\%$.
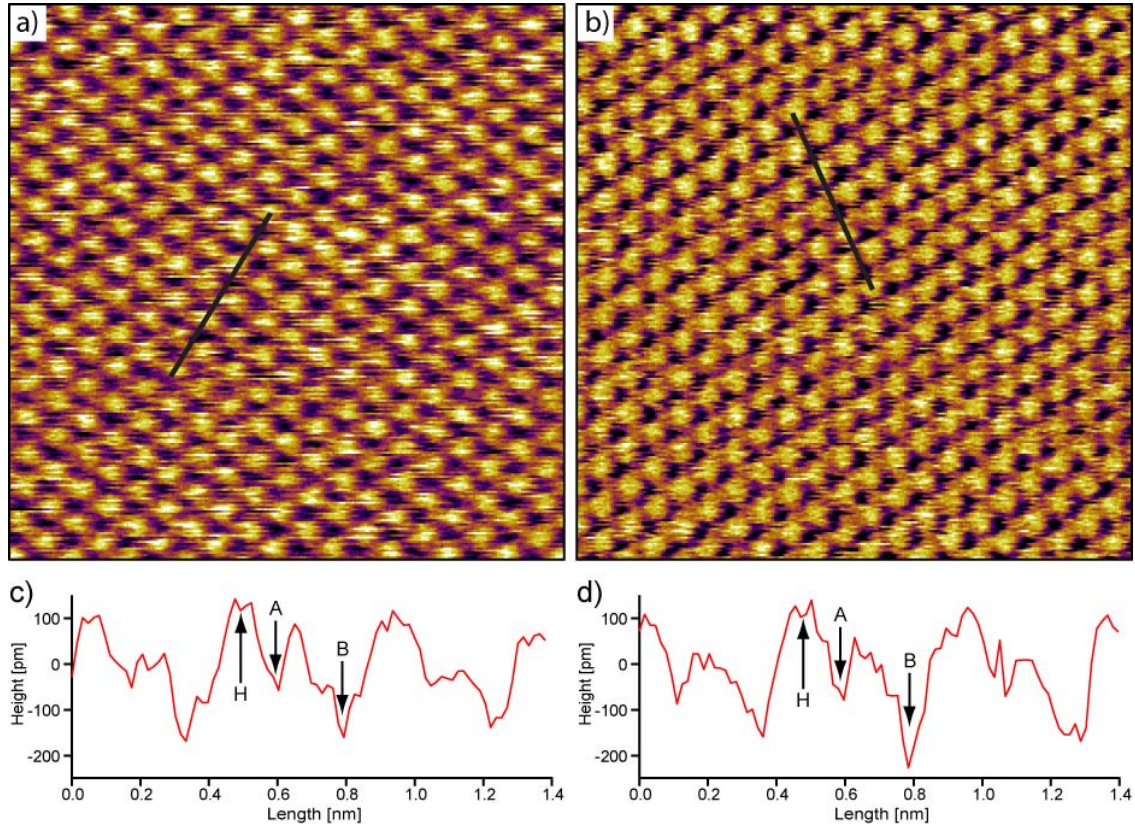
Figure 4. 4×4 nm images of HOPG collected in glycerol/water (70/30) using a) AM and b) FM modes. (Z scale = 300 pm, tip velocity $\sim$ 20 nm/s, $f_1 = 883 \pm 3$ kHz, $k_1 = 1779 \pm 451$ N/m, $Q_1 = 2.25 \pm 0.05$, $Q_C = 442$, $B = 1$ kHz). For AM imaging, the amplitude setpoint was $\Delta A_1 = 67$ pm and for FM the frequency setpoint was $\Delta f_1 = 110$ Hz with an amplitude of $A_1 = 60$ pm. AM roughness = 76 pm (RMS). FM roughness = 82 pm (RMS). Lattice spacings, λ_D, are slightly asymmetrical due to scanner compression in the images and were determined by 2D FFT. $\lambda_D^{AM} = 246$ pm and 245 pm, $\lambda_D^{FM} = 240$ pm and 236 pm, similar to a previously reported lattice constant of 246 pm [53]. c) and d) section graphs corresponding to the black lines in a) and b), respectively. The graphite honeycomb pattern is inverted by the imaging process with the highest points, H, corresponding to middle of hollow sites and A and B corresponding to different carbon atom sites.
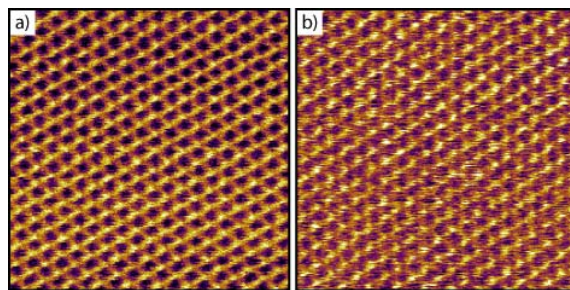
Figure 5. Corresponding energy dissipation using data from figure 4. (a) Calculated energy dissipation from AM mode (mean ~ 1.7 pW, Z scale = 20 fW). The average imaging amplitude was used for the calculations. b) Measured energy dissipation from FM mode (mean ~ 0.59 V, Z scale = 10 mV).
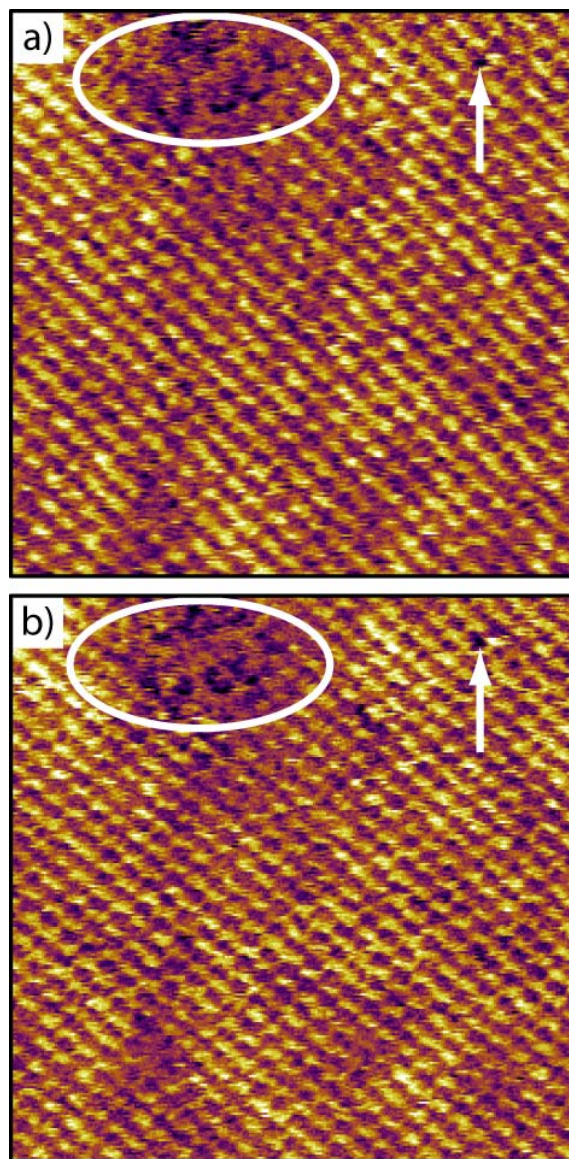
Figure 6. 10 x 10 nm FM mode images of a mica surface in a 70/30 glycerol/water solution. a) and b) show two subsequently recorded images exhibiting persistent defects and thus demonstrating true atomic resolution (amplitude ~ 0.2 nm, tip velocity ~ 50 nm/s, imaging time = 128 seconds per frame, Z scale = 250 pm).

REFERENCES

[1] Domanski A L, Sengupta E, Bley K, Untch M B, Weber S A L, Landfester K, Weiss C K, Butt H-J and Berger R 2012 *Langmuir* **28** 13892-9
[2] Jones R E and Hart D P 2005 *Tribol. Int.* **38** 355-61
[3] Hiasa T, Kimura K and Onishi H 2012 *J. Phys. Chem. C* **116** 26475-9
[4] O'Shea S J and Welland M E 1998 *Langmuir* **14** 4186-97
[5] Labuda A and Grütter P 2012 *Langmuir* **28** 5319-22
[6] Wishart J F 2009 *Energy Environ. Sci.* **2** 956-61
[7] Kim T Y, Lee H W, Stoller M, Dreyer D R, Bielawski C W, Ruoff R S and Suh K S 2010 *ACS Nano* **5** 436-42
[8] Zhu Y, *et al.* 2011 *Science* **332** 1537-41
[9] Ishikawa M, Sugimoto T, Kikuta M, Ishiko E and Kono M 2006 *J. Power. Sources* **162** 658-62
[10] Black J M, *et al.* 2013 *Nano Lett.* **13** 5954-60
[11] Fukuma T and Jarvis S P 2006 *Rev. Sci. Instrum.* **77** 043701
[12] Giessibl F J and Quate C F 2006 *Phys. Today* **59** 44-50
[13] Minary-Jolandan M, Tajik A, Wang N and Yu M-F 2012 *Nanotechnology* **23** 235704
[14] Melcher J, Martínez-Martín D, Jaafar M, Gómez-Herrero J and Raman A 2013 *Beilstein J. Nanotechnol.* **4** 153-63
[15] Fukuma T, Higgins M J and Jarvis S P 2007 *Phys. Rev. Lett.* **98** 106101
[16] Rode S, Oyabu N, Kobayashi K, Yamada H and Kühnle A 2009 *Langmuir* **25** 2850-3
[17] Loh S-H and Jarvis S P 2010 *Langmuir* **26** 9176-8
[18] Sheikh K H, Giordani C, Kilpatrick J I and Jarvis S P 2011 *Langmuir* **27** 3749-53
[19] Kilpatrick J I, Loh S-H and Jarvis S P 2013 *J. Am. Chem. Soc.* **135** 2628-34
[20] Ido S, Kimura K, Oyabu N, Kobayashi K, Tsukada M, Matsushige K and Yamada H 2013 *ACS Nano* **7** 1817-22
[21] Labuda A, Kobayashi K, Suzuki K, Yamada H and Grütter P 2013 *Phys. Rev. Lett.* **110** 066102
[22] Carda–Broch S, Berthod A and Armstrong D W 2003 *Anal. Bioanal. Chem.* **375** 191-9
[23] Toshio A 2012 *Nanotechnology* **23** 062001
[24] Sader J E 1998 *J. Appl. Phys.* **84** 64-76
[25] Naik T, Longmire E K and Mantell S C 2003 *Sens. Actuators A* **102** 240-54
[26] Albrecht T R, Grütter P, Horne D and Rugar D 1991 *J. Appl. Phys.* **69** 668-73
[27] Smith D P E 1995 *Rev. Sci. Instrum.* **66** 3191-5
[28] Giessibl F J, Bielefeldt H, Hembacher S and Mannhart J 1999 *Appl. Surf. Sci.* **140** 352-7
[29] Kobayashi K, Yamada H and Matsushige K 2009 *Rev. Sci. Instrum.* **80** 043708
[30] Colchero J, Cuenca M, Gonzalez Martinez J F, Abad J, Perez Garcia B, Palacios-Lidon E and Abellan J 2011 *J. Appl. Phys.* **109** 024310
[31] Ekinci K L, Yang Y T and Roukes M L 2004 *J. Appl. Phys.* **95** 2682-9
[32] Kim S-J, Ono T and Esashi E 2006 *Appl. Phys. Lett.* **88** 053116
[33] Dufour I, Lochon F, Heinrich S M, Josse F and Rebiere D 2007 *IEEE Sens. J.* **7** 230-6
[34] Giessibl F. Principle of NC-AFM. In: Morita S, Wiesendanger R, Meyer E, editors. Noncontact Atomic Force Microscopy: Springer Berlin Heidelberg; 2002. p. 11-46.
[35] Xu X and Raman A 2007 *J. Appl. Phys.* **102** 034303
[36] Kokavecz J and Mechler A 2007 *Appl. Phys. Lett.* **91** 023113
[37] Labuda A, Kobayashi K, Kiracofe D, Suzuki K, Grütter P H and Yamada H 2011 *AIP Adv.* **1** 022136
[38] Kiracofe D and Raman A 2011 *Nanotechnology* **22** 485502

[39] Kobayashi K, Yamada H and Matsushige K 2011 *Rev. Sci. Instrum.* **82** 033702
[40] Lübbe J, Temmen M, Rode S, Rahe P, Kühnle A and Reichling M 2013 *Beilstein J. Nanotechnol.* **4** 32-44
[41] García R and Pérez R 2002 *Surf. Sci. Rep.* **47** 197-301
[42] Butt H J and Jaschke M 1995 *Nanotechnology* **6** 1
[43] Pfeiffer O*, et al.* 2000 *Appl. Surf. Sci.* **157** 337-42
[44] Fukuma T, Onishi K, Kobayashi N, Matsuki A and Asakawa H 2012 *Nanotechnology* **23** 135706
[45] Giessibl F J 2003 *Rev. Mod. Phys.* **75** 949-83
[46] Fukuma T, Kilpatrick J I and Jarvis S P 2006 *Rev. Sci. Instrum.* **77** 123703
[47] Kilpatrick J I, Gannepalli A, Cleveland J P and Jarvis S P 2009 *Rev. Sci. Instrum.* **80** 023701
[48] Cheng N-S 2008 *Ind. Eng. Chem. Res.* **47** 3285-8
[49] Sader J E, Chon J W M and Mulvaney P 1999 *Rev. Sci. Instrum.* **70** 3967-9
[50] Higgins M J, Proksch R, Sader J E, Polcik M, Mc Endoo S, Cleveland J P and Jarvis S P 2006 *Rev. Sci. Instrum.* **77** 013701
[51] Melcher J, Hu S and Raman A 2007 *Appl. Phys. Lett.* **91** 053101
[52] Allers W, Schwarz A, Schwarz U D and Wiesendanger R 1999 *Appl. Surf. Sci.* **140** 247-52
[53] Hölscher H, Allers W, Schwarz U D, Schwarz A and Wiesendanger R 2000 *Phys. Rev. B.* **62** 6967-70
[54] Sader J E and Jarvis S P 2006 *Phys. Rev. B.* **74** 195424
[55] Anczykowski B, Gotsmann B, Fuchs H, Cleveland J P and Elings V B 1999 *Appl. Surf. Sci.* **140** 376-82
[56] Suzuki K, Oyabu N, Kobayashi K, Matsushige K and Yamada H 2011 *Appl. Phys. Express* **4** 125102
[57] Albrecht T R and Quate C F 1987 *J. Appl. Phys.* **62** 2599-602
[58] Marti O, Drake B and Hansma P K 1987 *Appl. Phys. Lett.* **51** 484-6
[59] Schultz S G and Solomon A K 1961 *J. Gen. Physiol.* **44** 1189-99
[60] Fukuma T, Ueda Y, Yoshioka S and Asakawa H 2010 *Phys. Rev. Lett.* **104** 016101
[61] Israelachvili J and Wennerstrom H 1996 *Nature* **379** 219-25
[62] Israelachvili J N and Pashley R M 1983 *Nature* **306** 249-50
[63] Roters A and Johannsmann D 1996 *J. Phys.: Condens. Matter* **8** 7561
[64] Fukuma T 2009 *Rev. Sci. Instrum.* **80** 023707
[65] Han W, Lindsay S M and Jing T 1996 *Appl. Phys. Lett.* **69** 4111-3
[66] Zhang J, Czajkowsky D M, Shen Y, Sun J, Fan C, Hu J and Shao Z 2013 *Appl. Phys. Lett.* **102** 073110
[67] Tamayo J, Humphris A D L and Miles M J 2000 *Appl. Phys. Lett.* **77** 582-4
[68] Kim J, Sung B, Kim B I and Jhe W 2013 *J. Appl. Phys.* **114** 054302
[69] Tamayo J 2005 *J. Appl. Phys.* **97** 044903
[70] Ashby P D 2007 *Appl. Phys. Lett.* **91** 254102
[71] Elmer F-J and Dreier M 1997 *J. Appl. Phys.* **81** 7709-14
[72] Eysden C A V and Sader J E 2007 *J. Appl. Phys.* **101** 044908
[73] Walters D A, Cleveland J P, Thomson N H, Hansma P K, Wendman M A, Gurley G and Elings V 1996 *Rev. Sci. Instrum.* **67** 3583-90